

Preparation and Microstructural Investigation of the High- T_c Superconductor $\text{Pb}_2\text{Sr}_2\text{Y}_{0.5}\text{Ca}_{0.5}\text{Cu}_3\text{O}_{8+\delta}$ *

T. J. White,^A Z. Barnea, P. Goodman and D. G. Jensen

School of Physics, University of Melbourne,
Parkville, Vic. 3052, Australia.

^A National Advanced Materials Analytical Centre,
University of Melbourne,
Parkville, Vic. 3052, Australia.

Abstract

Simple conditions for the preparation of the high- T_c superconductor $\text{Pb}_2\text{Sr}_2\text{Y}_{0.5}\text{Ca}_{0.5}\text{Cu}_3\text{O}_{8+\delta}$ in single phase are given. High resolution electron microscope studies of this material confirm the basic orthorhombic structure having C_{mmm} symmetry. Overlaying this structure is a perturbation due to random displacements of Pb from the ideal square-symmetric sites, attributed to a randomness in oxygen sub-stoichiometry. This and the absence of superstructure ordering appears to characterise the superconducting form of this compound.

1. Introduction

The synthesis method for high- T_c superconducting ceramics whereby a base matrix precursor prepared from ceramic oxides is reacted with a lower melting constituent (Gopalakrishnan *et al.* 1988) has permitted the preparation of a wide range of quaternary and quinary compounds. As a result, several new superconducting materials have been discovered (e.g. Ganguli *et al.* 1987; Liu *et al.* 1987). Following this technique, Cava *et al.* (1988) systematically explored a distinct class of high- T_c superconductors having the stoichiometry $\text{Pb}_2\text{Sr}_2\text{ACu}_3\text{O}_{8+\delta}$. Neither lanthanide (Ln) endmembers (namely $\text{Pb}_2\text{Sr}_2\text{LnCu}_3\text{O}_8$) nor oxygen-rich compounds ($0 < \delta \leq 1.8$) were superconductors. However, coupled substitution of alkali earth elements (Ca, Sr) with lanthanides or yttrium yielded superconducting compounds, having the general formula $\text{Pb}_2\text{Sr}_2\text{Ln}_{1-x}(\text{Ca}, \text{Sr})_x\text{Cu}_3\text{O}_{8+\delta}$. Those phases with optimal superconducting properties had $x \sim 0.5$ and $\delta \sim 0$. The Ba analogues of this material have since been made (Rouillon *et al.* 1989).

In common with other superconducting oxides, the crystal structures of these compounds consist of perovskite-like slabs interleaved with rocksalt-type layers (Fig. 1). Both superconducting and semiconducting phases are believed to possess orthorhombic (C_{mmm}) symmetry, in which the relationship to the perovskite archetype ($a_0 \sim 3.85 \text{ \AA}$) is reflected in the supercell dimensions ($a' = \sqrt{2}a_0$ and $c' = 4a_0$). In $\text{Pb}_2\text{Sr}_2\text{Y}_{0.5}\text{Ca}_{0.5}\text{Cu}_3\text{O}_8$ the lead atoms are in square pyramidal coordination to oxygen and separated along c by Cu^{1+} ions in linear coordination (when $\delta = 0$). It has been suggested (Cava *et al.* 1989)

* Paper presented at the DITAC Conference on Superconductivity held in Canberra, 13-14 February 1989.

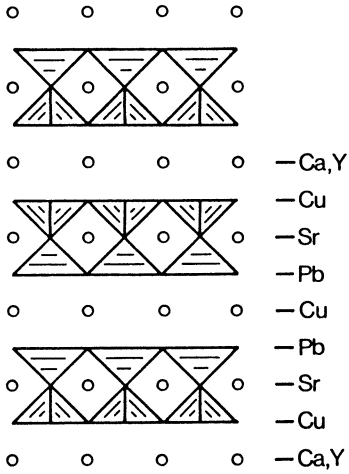


Fig. 1. Schematic illustration of polyhedral topology in $Pb_2Sr_2Y_{0.5}Ca_{0.5}Cu_3O_8$ viewed along [110].

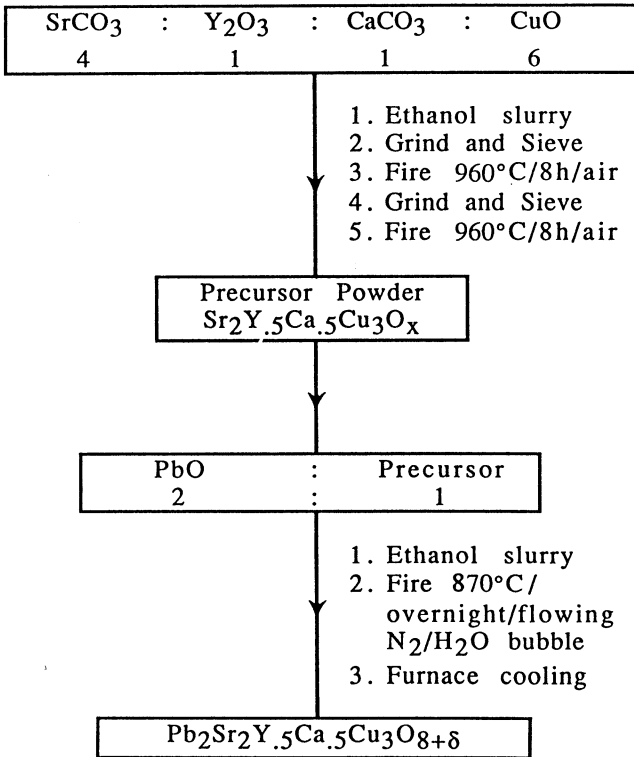


Fig. 2. Flow chart for fabrication of $Pb_2Sr_2Y_{0.5}Ca_{0.5}Cu_3O_{8+\delta}$.

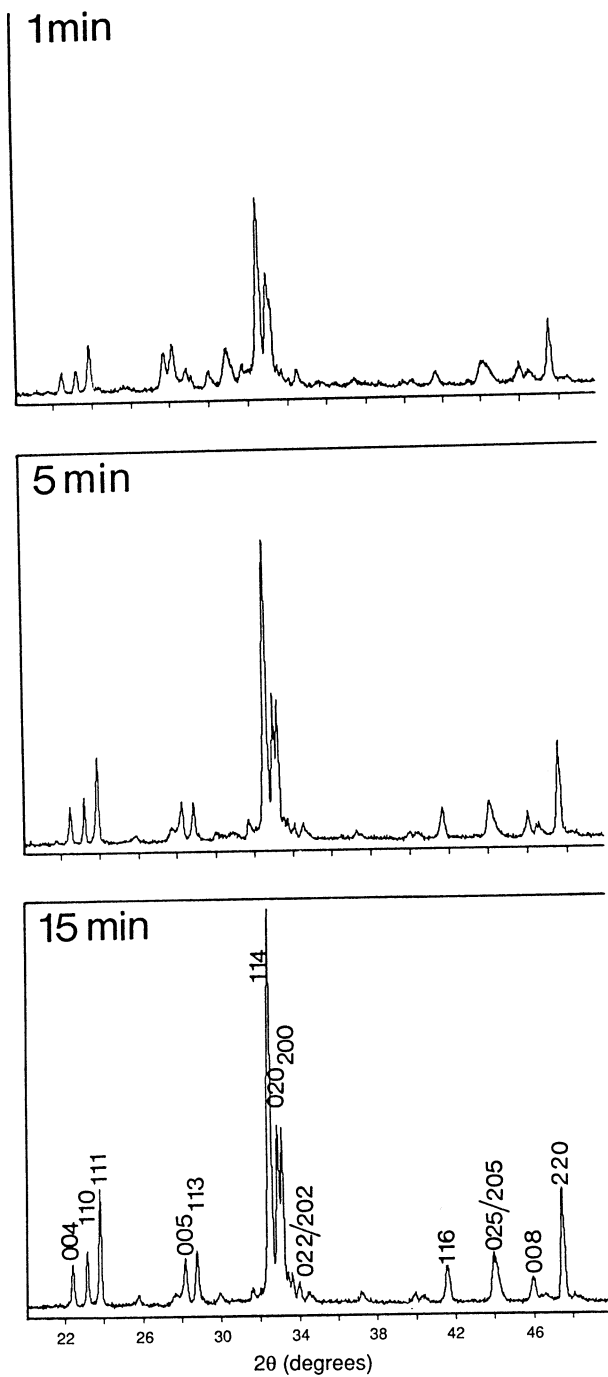


Fig. 3. Powder XRD pattern showing the effect of growth with respect to firing time.

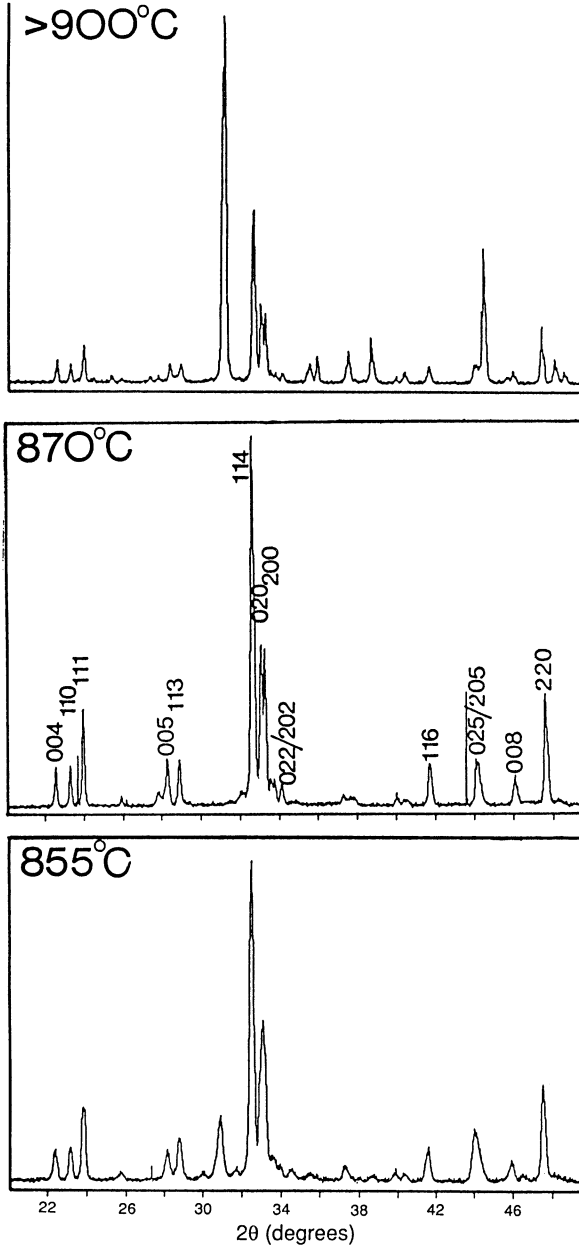


Fig. 4. Powder XRD pattern showing phase development with respect to temperature.

that the oxygen content of these CuO_δ chains is variable and that they act as electron acceptors which induce the holes necessary for superconductivity in the CuO_δ pyramidal planes. Strontium, calcium and rare-earth atoms fill the larger interstices (8 or 9 coordination) between the CuO_δ polyhedra. In detail however, the structure is likely to be more complex. Recent analysis indicates that the contentious space group issue is still unresolved (Cava *et*

al. 1989; Subramaniam *et al.* 1989). Although the orthorhombic cell gave a good fit to the powder X-ray diffraction (XRD) data, a shoulder on the (314) reflection could be indicative of monoclinic symmetry. This was substantiated by electron diffraction which showed that some crystals violate the C-centring of the orthorhombic structure and reveal ordered superlattices in the (001) planes.

To clarify the question of symmetry and investigate the degree of cation ordering we undertook a high resolution electron microscope investigation of $\text{Pb}_2\text{Sr}_2\text{Y}_{0.5}\text{Ca}_{0.5}\text{Cu}_3\text{O}_{8+\delta}$. Atomic resolution images of this material reveal atomic disorder and local substructure which have been undetected by X-ray diffraction or conventional electron microscopy. Minor quantities of a disordered, probably metastable polytypoid were also found. We believe that this phase provides clues to the mechanisms of crystal growth via systematic topological rearrangement of perovskite polytypes.

Table 1. Calculated and experimental XRD data for $\text{Pb}_2\text{Sr}_2\text{Y}_{0.5}\text{Ca}_{0.5}\text{Cu}_3\text{O}_{8+\delta}$

<i>hkl</i>	Calculated <i>d</i> (Å)	<i>I</i> / <i>I</i> ₀	Experimental <i>d</i> (Å)	<i>I</i> / <i>I</i> ₀	<i>hkl</i>	Calculated <i>d</i> (Å)	<i>I</i> / <i>I</i> ₀	Experimental <i>d</i> (Å)	<i>I</i> / <i>I</i> ₀
004	3.9543	5	3.939	12	202	2.5700	<1		
110	3.8530	5	3.815	12	115	2.4449	<1		
111	3.7435	28	3.707	27	023	2.4253	1	2.407	4
			3.436	5	203	2.4155	1	2.387	4
			3.206	5	007	2.596	<1	2.251	5
005	3.1634	9	3.153	14	024	2.2474	<1		
113	3.1108	5	3.084	14	204	2.2396	<1		
			2.780	5	116	2.1757	13	2.164	13
114	2.7596	100	2.740	100	025	2.0674	10	2.049	13
020	2.7315	32			008	1.9771	5	1.965	7
200	2.7175	32	2.706	44	117	1.9491	<1		
021	2.6917	3	2.690	43	220	1.9265	19	1.909	31
201	2.6783	2	2.666	9	221	1.9124	<1		
006	2.6362	2	2.652	8	026	1.8969	<1		
112	2.5818	<1	2.625	7	206	1.8922	<1		
022	2.581	<1							

2. Experimental

(a) Fabrication

Stoichiometric quantities of SrCO_3 , Y_2O_3 , CaCO_3 and CuO were mixed and fired at 960°C to yield a precursor powder of composition $\text{Sr}_2\text{Y}_{0.5}\text{Ca}_{0.5}\text{Cu}_3\text{O}_x$ (see Fig. 2). PbO was slurried with the precursor in the molar ratio of 2 : 1 and fired in a stream of N_2 saturated with water vapour. Various combinations of firing time (see Fig. 3) and temperature (see Fig. 4) were tried in order to find the optimum conditions to obtain a single-phase sample. It was found that a maximum yield resulted when fired at $870\pm 10^\circ\text{C}$ for periods of >15 min. In powder form, the reaction is driven to completion extremely quickly. On the other hand, pellets require longer reaction times to obtain a homogeneous product. A comparison of calculated and experimental XRD data for $\text{Pb}_2\text{Sr}_2\text{Y}_{0.5}\text{Ca}_{0.5}\text{Cu}_3\text{O}_{8+\delta}$ is shown in Table 1. Four-terminal resistivity measurements revealed the high temperature ramp with a resistivity turnover at 71 K, as reported by Cava *et al.* (1988).

(b) Electron Microscopy

Specimens were prepared for electron microscopy by crushing in a mixture of ethanol and liquid N_2 to make a suspension that was dried onto holey carbon films. Selected area electron diffraction (SAD), conventional electron microscopy and scanning electron microscopy (SEM) were conducted using a JEM 2000FX electron microscope operated at 200 keV. Atomic resolution electron microscopy was carried out with a JEM 4000EX instrument operated at 400 keV and having manufacturer specified coefficients of spherical aberration C_s and chromatic aberration C_c of 1.0 and 1.7 mm respectively. The Scherzer crossover was calculated to be near -400 \AA . The objective aperture included all diffracted beams within a radius of 1.4 \AA^{-1} . Experimental high-resolution images were interpreted by visual comparison with simulated images computed by multi-slice methods. For image simulation a beam divergence of 3 mrad was used and the defect-of-focus taken as 80 \AA . Beam tilt and objective lens astigmatism were assumed to be negligible. These conditions were adequate to directly interpret structurally defective regions.

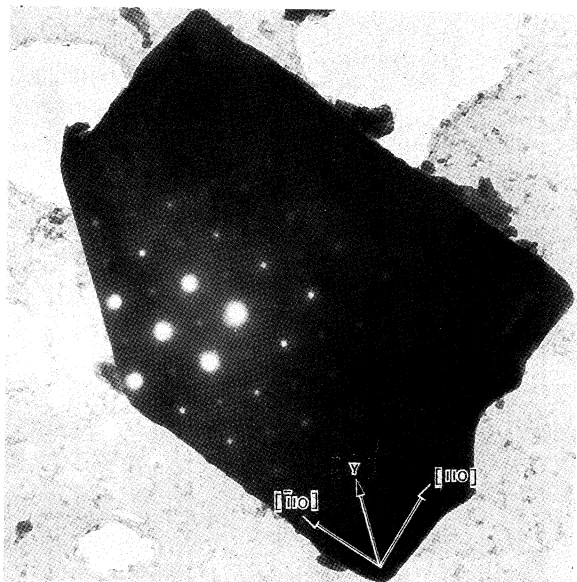


Fig. 5. Bright field transmission electron microscope images of crystal fragment supported on a holey carbon film. The corresponding $[001]$ selected area electron diffraction (SAD) pattern overlays the crystal.

(c) Morphology

$Pb_2Sr_2Y_{0.5}Ca_{0.5}Cu_3O_{8+\delta}$ showed strong cleavage on the $\{110\}$ planes (equivalent to $\{100\}$ of the cubic archetype) giving rise to characteristic equant tablets. An example of one such fragment and its corresponding SAD pattern is given in Fig. 5. The secondary electron image of the crystal is shown in Fig. 6a. When tilted about $[110]$ (Fig. 6b) the tabular nature is emphasised and shows the crystal to be micaceous with (001) cleavage. Observations by high resolution

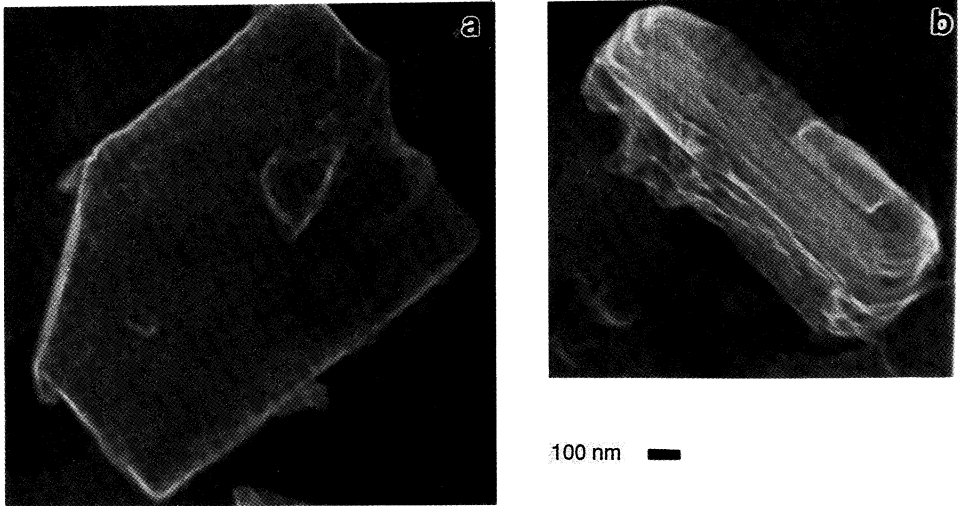


Fig. 6. Secondary electron image of the same crystal as in Fig. 5: (a) [001] orientation; (b) tilted about [110] to expose micaceous nature of fragments.



Fig. 7. Intercalation of an amorphous region in a monocrystal.

electron microscopy reveal these micaceous sheets to be bonded together by amorphous filling some 30–50 Å in extent. Fig. 7 is a typical example of this phenomenon where two crystalline regions are joined by an amorphous strip parallel to (110).

(d) Electron Beam Damage

Although the superconductor was reasonably stable in the electron beam, atomic disorder and amorphisation occurred when observations were continued for extended periods (>15–20 min). This is illustrated in Fig. 8 where [110] atomic resolution images of the same area were recorded approximately 10 min apart. The image in Fig. 8*a* is extremely regular indicative of well ordered atomic columns. However, after continuous observation (Fig. 8*b*) electron beam induced disorder is apparent, manifesting itself as misplaced atomic columns or an absence of crystalline order.

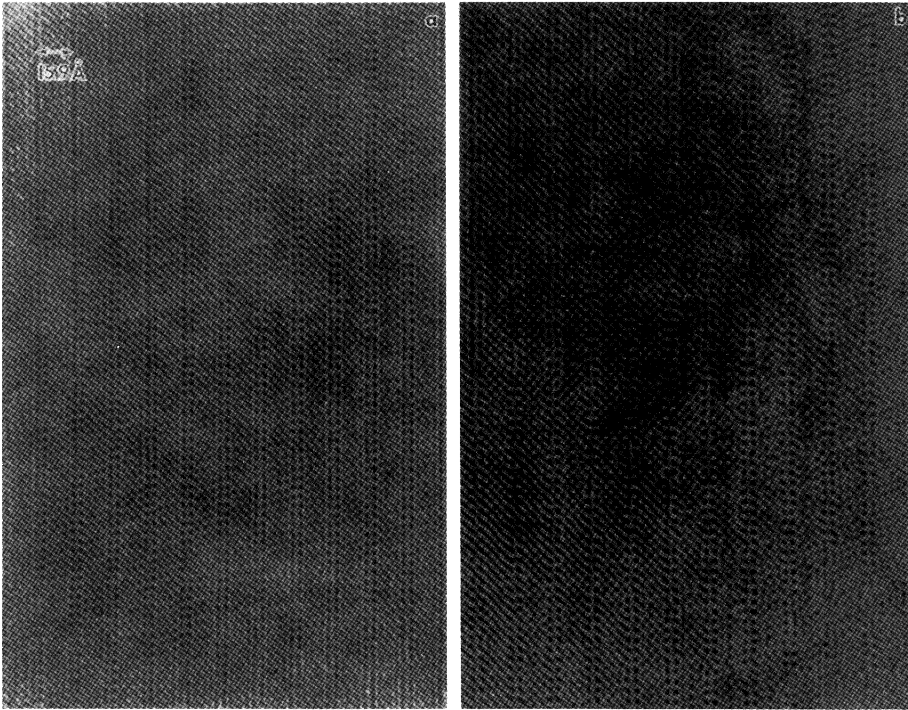


Fig. 8. (a) [110] image after short exposure (<5 min) to a 400 keV electron beam. (b) Same area after 15 min exposure.

3. Discussion of Results

Since electronic properties are likely to be sensitive to both partially periodic and aperiodic departures from the idealised C_{mmm} structure, it is of some interest to identify and classify static disorder which can be recognised in freshly examined crystals, free from radiation effects. Disorder is described below for [110] and [001] projections.

(a) Disorder in $[110]_{\text{ortho}} = \langle 100 \rangle_{\text{cubic}}$ subcell

High resolution images taken in the $[110]$ direction permit direct observation (i.e. unobscured by parallax) of the cation layering sequence along c (see Fig. 1). Using the crystal data given by Cava *et al.* (1988), we calculated a through focal series (TFS) for a crystal slice 18 \AA thick (Fig. 9). Images of maximum contrast occur at foci from -300 to -400 \AA (under these conditions black dots correspond to homoatomic columns). The TFS in Fig. 10 calculated for the optimum defocus setting of -300 \AA demonstrates that directly interpretable images can be obtained up to thicknesses of 36 \AA .

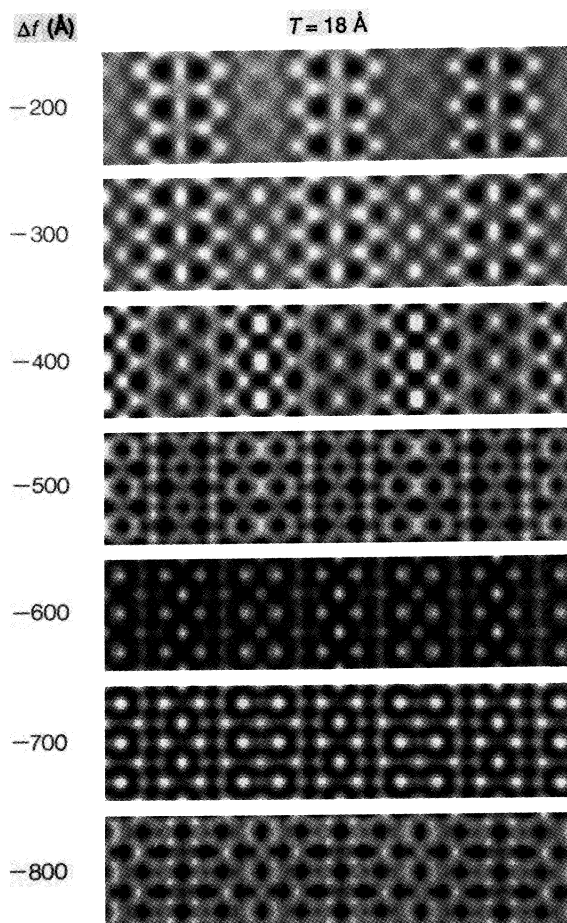


Fig. 9. Calculated images at various defects of focus Δf for a $[110]$ projection $T = 18 \text{ \AA}$ thick.

Fig. 11a is an atomic resolution micrograph of the $[110]$ projection in which the double row of Pb atoms forms the dominant feature, delineating the 15.8 \AA c -axis. However, the multi-slice image match (inset to Fig. 11a) although in broad agreement with the experimental images shows a number of important discrepancies. In particular, the square arrangement of the Pb

atoms (separated by a Cu atom) is usually disordered. This may reflect the partial oxidation of Cu and the presence of countervalent oxygen which would randomly induce local relaxation in the structure. Furthermore, the intensity of the strontium layer is variable, presumably due to partial replacement by Ca.

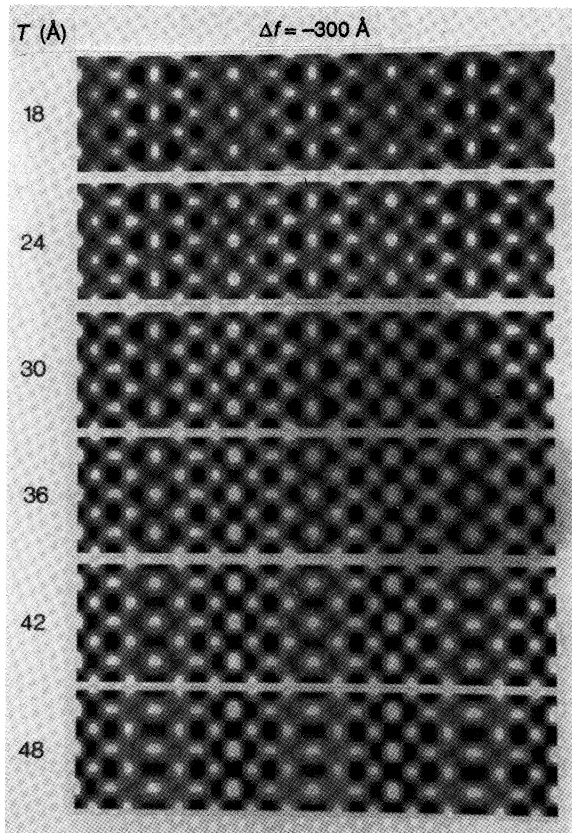


Fig. 10. Through-thickness $[110]$ images calculated at -300 \AA , the optimum defect of focus.

(b) Disorder in $[001]_{\text{ortho}} = [001]_{\text{cubic subcell}}$

Fig. 12 is a simulated TFS for the $[001]$ projection in which a crystal thickness of 30 \AA (i.e. two unit cells) was assumed. Over a defect of focus -200 to -400 \AA the image is rather constant with black dots showing a one-to-one correspondence with cationic columns. Beyond $\Delta f = -400 \text{ \AA}$ the image becomes more complex and is not directly interpretable.

The experimental $[001]$ micrograph shown in Fig. 11*b* displays little of the regularity associated with the simulation. Rather, it contains microdomains of regular structure separated by regions exhibiting two distinct types of disorder. The first of these (A in Fig. 11*b*) is directional disorder along $\langle 110 \rangle$. This was also detected in SAD patterns as $\langle 110 \rangle$ streaks; however, we failed to observe the ordered superstructures alluded to by Cava *et al.* (1988). Because streaking occurs in one direction only, disorder may be favoured either along $[110]$ or $[\bar{1}10]$, but the small difference between these spacings has prevented confirmation

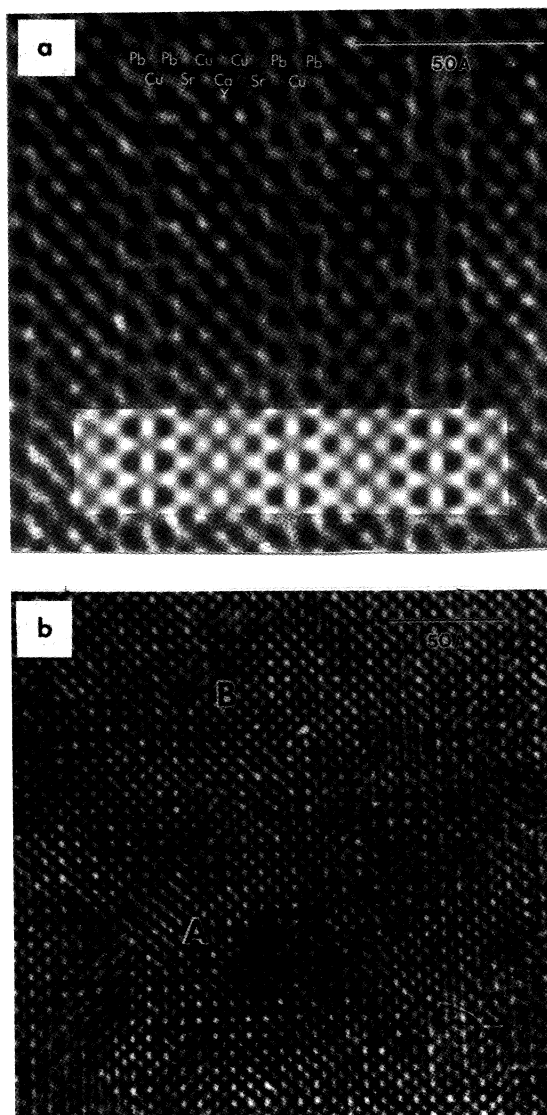


Fig. 11. (a) Atomic resolution image of $\text{Pb}_2\text{Sr}_2\text{Y}_{0.5}\text{Ca}_{0.5}\text{Cu}_3\text{O}_{8+\delta}$ viewed in the [110] direction. Black dots correspond to cation columns. The inset shows an image calculated using the following parameters: $\Delta f = -300 \text{ \AA}$, crystal thickness of 18 \AA , $C_s = 1.0 \text{ mm}$, divergence of illumination of 3.0 mrad and objective aperture radius of 1.4 \AA^{-1} . (b) Atomic resolution image of the [001] zone showing linear defects (A) and disordered microdomains (B).

of this. As a consequence of the fact that $\langle 110 \rangle$ planes are equivalent to $\{001\}$ pseudo-cubic planes on which long-range ordering is superimposed, supercells can develop on any of these planes, and partial ordering can occur in three dimensions. After significant ordering has occurred (sufficient to clearly delineate the supercell dimensions) air quenching immobilises local microdomains of partial order or disorder. Naturally, this leads to defects of type B which are highly disordered and reflect extremes in local stoichiometry unfavourable to perovskite coordination.

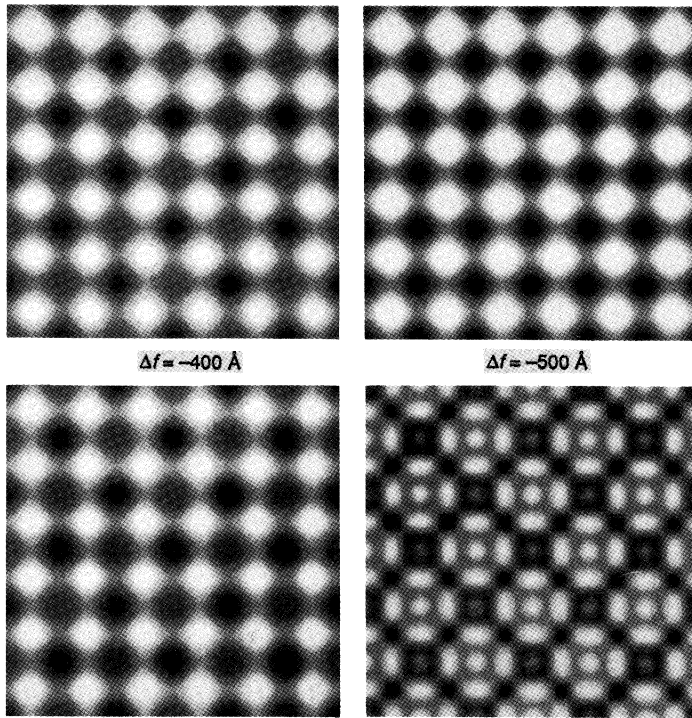


Fig. 12. Calculated TFS for the [001] zone at a thickness of $T = 30 \text{ \AA}$.

4. Phase Development via Crystallochemical Rearrangement

The 'building block' approach to the fabrication of ceramics was instigated partly to minimise the formation of secondary phases in chemically complex systems, and also to reduce volatilisation of low melting point oxides (e.g. PbO , Tl_2O_3 and Bi_2O_3). A feature of these preparative techniques, which has not yet received significant attention, is the reconstructive transformations that occur as the precursor structure incorporates new components. An understanding of these phenomena will allow the prediction of growth mechanisms, facilitate the preparation of new polytypoids and suggest methods to maximise the quantity of metastable (but possibly superconducting) polytypoids.

In the present case crystals could be identified which were the result of partial reaction between PbO and the precursor. High resolution analyses of these intermediate compounds allow the sequence of the solid state reaction to be followed, sometimes in a single field of view.

Fig. 13 shows the diagnostic [110] (or the [001] tetragonal equivalent) of a region containing an intermediate phase with K_2NiF_4 topology. This intergrowth structure vividly illustrates the structural relationships between perovskite polytypoids (K_2NiF_4 -type and the precursor), and may provide a key to the mechanisms by which one structure transforms to another. The central portion of the micrograph conforms to a material having the usual K_2NiF_4 -type structure, and is similar to materials described by Michel and Raveau (1984) in the La-Cu-oxide system. On the left of Fig. 13 is a single

bright row of dots resulting from the replacement of a single Cu plane by Pb atoms, whilst on the right this process has led to a perfectly ordered (possibly metastable) polytypoid. Despite the contrast variations across this field of view, K_2NiF_4 -type topology is maintained.

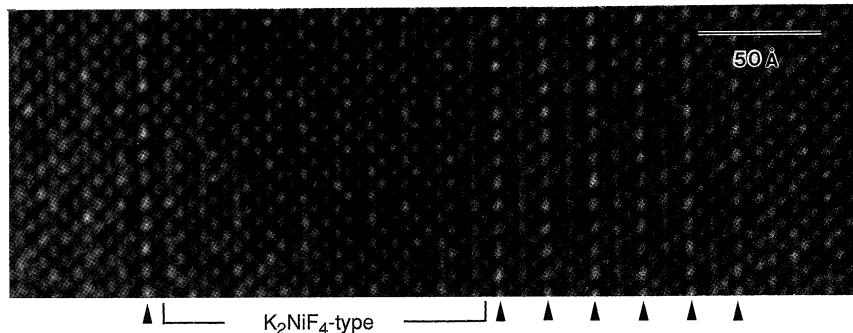


Fig. 13. Micrograph showing both isolated and ordered replacement of Cu by planes of Pb atoms in an intermediate structure. Beneath we indicate a region of K_2NiF_4 structure, while the arrowheads indicate rows of Pb atoms in the structure.

In the present case, the isolated planes of Pb atoms in the intermediate K_2NiF_4 -type demonstrate that incorporation of this species occurs by solid state diffusion on (001) planes possibly during the reconstructive transformation of the 1-2-3 precursor compound. It seems likely that this phenomenon will be applicable to other superconductor syntheses routes where 'building block' precursor compounds are used and that high resolution electron microscopy will play a key role deciphering the mechanisms of crystal growth.

References

- Cava, R. J., *et al.* (1988). *Nature* **336**, 211.
 Cava, R. J., *et al.* (1989). *Physica C* **157**, 272.
 Ganguli, A. K., Nanjundaswamy, K. S., and Rao, C.N.R. (1987). *Physica C* **156**, 788.
 Gopalakrishnan, I. K., *et al.* (1988). *Appl. Phys. Lett.* **53**, 414.
 Liu, R. S., Huang, Y. T., Lee, W. H., Wu, S. F., and Wu, P. T. (1987). *Physica C* **156**, 791.
 Michel, C., and Raveau, B. (1984). *Rev. Chim. Min.* **21**, 407.
 Rouillon, T., *et al.* (1989). *J. Sol. State Chem.* **78**, 322.
 Subramaniam, M. A., *et al.* (1989). *Physica* **157**, 124.

